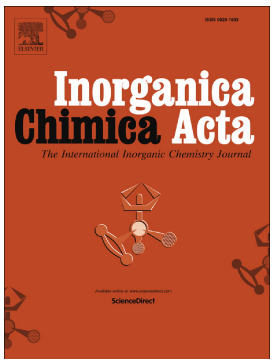

A water-soluble Schiff base ligand and its Al(III) complex: optical properties, computational studies and photocatalytic performance

Hajer Bouznif, Licínia L.G. Justino, Telma Costa, Maria I.L. Soares, M. Luísa Ramos, Teresa M.V.D. Pinho e Melo, Nabil Zouari, Rui Fausto

PII: S0020-1693(25)00480-3

DOI: https://doi.org/10.1016/j.ica.2025.123014

Reference: ICA 123014

To appear in:

Received date: 29 October 2025

Revised date: 27 November 2025

Accepted date: 28 November 2025

Please cite this article as: H. Bouznif, L.L.G. Justino, T. Costa, et al., A water-soluble Schiff base ligand and its Al(III) complex: optical properties, computational studies and photocatalytic performance, (2024), https://doi.org/10.1016/j.ica.2025.123014

A water-soluble Schiff base ligand and its Al(III) complex: optical properties, computational studies and photocatalytic performance

Hajer Bouznif[1,2,*], Licínia L. G. Justino[2,*], Telma Costa[2], Maria I. L. Soares[2], M. Luísa Ramos[2], Teresa M. V. D. Pinho e Melo[2], Nabil Zouari[1] and Rui Fausto[2,3]

[1] *Laboratory Physico-Chemistry of the Solid State, Department of Chemistry, Faculty of Sciences of Sfax, B. P. 1171, Sfax 3000, University of Sfax, Tunisia*

[2] *CQC-IMS, Department of Chemistry, University of Coimbra, Rua Larga 3004-535 Coimbra, Portugal*

[3] *Spectroscopy@IKU, Faculty of Sciences and Letters, Department of Physics, Istanbul Kultur University, Ataköy Campus, Bakirköy 34156, Istanbul, Turkey*

Abstract

Although the field of inorganic photophysics and photochemistry has traditionally been dominated by complexes of precious and rare metals, increasing concerns regarding their scarcity and cost have led to a growing interest in earth-abundant metal-based compounds as more sustainable and economically viable alternatives. In this study, we investigated the photophysical properties of two water-soluble compounds: the di-Schiff base *N*,*N*′-bis(3-methoxy-5-sulfonatosalicylidene)-1,2-ethylenediamine disodium salt (**MSS**) and its corresponding Al(III) complex. To better understand the enol-imine (O-H···N) *vs.* keto-enamine (O···H-N) tautomeric behavior of **MSS**, we also considered its non-methoxy analogue (**SS**) as a reference compound. Using UV-vis absorption and diffuse reflectance spectroscopy, we examined the tautomeric preferences of **MSS** and **SS** in both the solid state and various solvents. The spectral features of **MSS** exhibited a noticeable bathochromic shift relative to **SS** in all media. In protic solvents (H_2O, MeOH) and in the solid state, **MSS** is found predominantly in the keto-enamine form, while in aprotic polar solvents (DMSO, DMF), a mixture of keto and enol forms coexist. In contrast, **SS** shows a dynamic coexistence of both tautomeric forms in protic solvents, while the **SS** enol form becomes dominant in DMSO and DMF; in the solid-state **SS** predominantly adopts the keto-enamine form. These differences were rationalized in terms of electronic effects. The direct band gap energies were determined to be 2.75 eV for **SS**, 2.61 eV for **MSS** and 3.03 eV for the **Al(III)/MSS** complex, revealing their wide-band-gap-semiconductor character. These values were supported by DFT calculations, which were found to be able to reproduce the experimental trends and were also used to provide insight into the electronic structure of the studied compounds. Photoluminescence analysis revealed that **MSS** emits in the green region, while the **Al(III)/MSS** complex exhibits a blue-white emission, making both compounds promising candidates for application in single-layer white OLEDs. Additionally, the **Al(III)/MSS** complex displayed photocatalytic activity toward the degradation of methylene blue (MB), with a rate constant (K) of 0.032 min^{-1}, indicating its potential as a multifunctional material for both optoelectronic and environmental applications.

Keywords: Water-soluble Schiff base; Keto-enol tautomerism; Al(III) complex; Photocatalytic activity; wide-band-gap semiconductors

Corresponding authors e-mails: bouznifhajer13@gmail.com (Hajer Bouznif), liciniaj@ci.uc.pt (Licínia L. G. Justino)

Introduction

Schiff bases, first synthesized in the mid-19th century [1], have been extensively studied due to their straightforward synthesis and relevance in various fields, such as optical chemical sensors [2], LEDs [3], and catalysis [4]. Among them, *salen*-type Schiff bases have attracted considerable interest due to their versatility and tunability. These compounds usually undergo easy intramolecular proton transfer between the azomethine nitrogen atom and the *ortho*-phenolic oxygen, resulting in two tautomeric structures: enol-imine and keto-enamine. The equilibrium between these tautomers is strongly influenced by the dielectric constant of the solvent, as well as electronic and steric factors [5–10]. The enol-imine and keto-enamine forms absorb light at different wavelengths [11], allowing their spectroscopic differentiation. In general, the keto-enamine tautomeric form is prevalent in polar solvents [12], resulting in the appearance of a broad absorption band above 400 nm [11,13], while the enol-imine form is predominantly observed in nonpolar solvents and is distinguished by its characteristic absorption at lower wavelengths [12]. Hydrogen bonding with protic solvents further stabilizes the keto-enamine form [7,14], as has been highlighted by Palusiak et al., who have also suggested that substituent effects and hydrogen-bond resonance assistance act cooperatively [15]. Despite extensive studies, the influence of solvent polarity and substituent characteristics on the enol-imine and keto-enamine tautomeric equilibrium in *salen*-type Schiff bases remains insufficiently understood and continues to be a topic of ongoing research and interest.

Recently, we synthesized and characterized a water-soluble di-Schiff base, *N*,*N*′-bis(3-methoxy-5-sulfonatosalicylidene)-1,2-ethylenediamine disodium salt (**MSS**) (Scheme 1) [16]. A detailed investigation of the enol-imine *vs.* keto-enamine tautomerism was conducted, along with an analysis of the role of intra- and intermolecular interactions in determining tautomeric preferences in different media. Based on theoretical calculations and condensed phase experimental studies, the enol-imine tautomeric form was found to be preferred in the gas phase, while the keto-enamine form was determined to be the predominant tautomer in water and DMSO, as well as in the solid state. To assess the stability of **MSS** against hydrolysis over time, we conducted a series of experiments and compared it with that of its non-methoxy substituted analogue, *N*,*N*′-bis(5-sulfonatosalicylidene)-1,2-ethylenediamine disodium salt (**SS**) (Scheme 1). The differences found were rationalized based on the different tautomeric equilibria of the two Schiff bases and the specific structural susceptibilities towards nucleophilic attack by water of their dominant tautomers. Subsequently, **MSS** was used in

complexation studies in aqueous solution and to synthesize a novel Al(III) complex in non-aqueous media (Scheme 1). This complex was found to have an octahedral geometry, according to NMR and DFT studies, and to be thermally stable up to 281 °C, as revealed by DSC studies. These results led us to consider the possibility of modifying the enol-imine *vs.* keto-enamine tautomeric equilibrium in these compounds by employing different substituents and exploring the influence of solvent dielectric effects on this equilibrium. Hence, in the present work, we have explored these topics for the two ligands, **SS** and **MSS**.

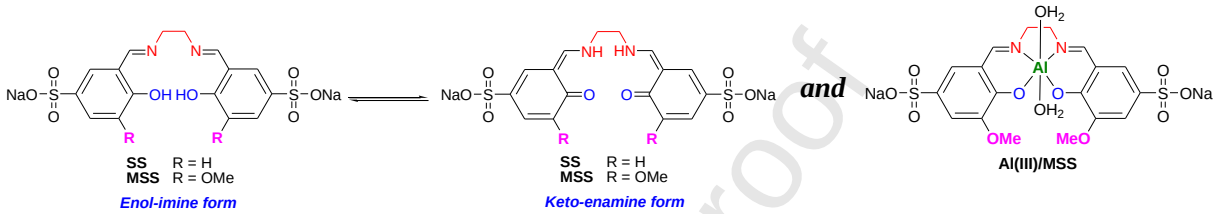

Scheme 1. Enol-imine and keto-enamine forms of water-soluble di-Schiff base ligands **SS** and **MSS**, and **Al(III)/MSS** complex [16].

In addition, the photophysical properties of **MSS** and its Al(III) complex were investigated in the present study. The band gap energy of the synthesized **Al(III)/MSS** complex was determined, revealing its wide band gap semiconductor character. These studies were motivated by the accumulated evidence that aluminum-based complexes, including those with Schiff bases, are suitable materials for application in optoelectronics [17–22]. Indeed, in the light of recent advances in this field, the photophysical behavior of our previously reported water-soluble **Al(III)/MSS** complex [16] represents a compelling avenue for further exploration.

Furthermore, we have explored the application of the **Al(III)/MSS** complex as an innovative photocatalyst for the degradation of the methylene blue (MB) dye. The objective of this study was to evaluate the effectiveness of the synthesized complex in breaking down MB under UV light exposure. MB is a popular cationic dye that is environmentally persistent, poisonous, carcinogenic, and mutagenic [23], and appropriate treatment of MB containing industrial effluents is garnering considerable attention. Various methods have been used to remove MB from aqueous solutions, including bioremediation [24], adsorption [25,26], and photodegradation [27]. Among these, photocatalytic degradation is considered the most promising approach, allowing for effective removal of the compound and producing safe end products, while being cost-effective and time-efficient [25,27–29].

Experimental and computational methods

Materials. Methylene blue ($C_{16}H_{18}ClN_3S$), ethylenediaminetetraacetic acid disodium salt 2-hydrate (EDTA), p-benzoquinone (BQ), ethanol (EtOH), millipore Milli-Q water, methanol (MeOH), dimethyl sulfoxide (DMSO), and dimethylformamide (DMF), were purchased from commercial suppliers and used as supplied or distilled.

Schiff bases **SS**, **MSS** and **Al(III)/MSS** complex were synthesized and characterized in our previous studies [16].

Physical Measurements. A Shimadzu 2600 UV-vis spectrophotometer and a Jobin-Yvon-Spex-Fluorolog 3–2.2 spectrofluorometer were used to record the UV-vis absorption and fluorescence spectra, respectively. The concentration of the samples used in the UV-vis studies was in the range of 1.0×10^{-5} mol dm^{-3} to 1.0×10^{-4} mol dm^{-3}. Fluorescence quantum yields have been measured utilizing quinine sulfate in 0.5 mol dm^{-3} sulfuric acid ($\phi_F^{ref} = 0.55$) [30] as standard and calculated using the following equation:

$$\emptyset_F = \frac{\int I_s(\lambda)d(\lambda)}{\int I_{ref}(\lambda)d(\lambda)} \cdot \frac{{OD_s}^2}{{OD_{ref}}^2} \cdot \frac{{n_s}^2}{{n_{ref}}^2} \cdot \emptyset_F{}^{ref} \quad (1)$$

where $\int I_s(\lambda)d(\lambda)$ and $\int I_{ref}(\lambda)d(\lambda)$ are the integrated area under the corrected emission spectra of the sample (s) and reference (ref) solutions. The solutions were optically matched at the excitation wavelength $\left(\frac{{OD_s}^2}{{OD_{ref}}^2} = 1\right)$, using water as solvent $\left(\frac{{n_s}^2}{{n_{ref}}^2} = 1\right)$ and DMSO as solvent $\left(\frac{{n_s}^2}{{n_{ref}}^2} = 1.23\right)$.

The ^{1}H NMR (400 MHz) spectra were acquired using a Bruker Avance III-400 NMR spectrometer, and the solutions were prepared in deuterium oxide D_2O (99.9% D).

A UV–vis–NIR light source (Mikropack DH-2000-BAL) with a fiber optic probe (FCR-UVIR 200/600–2-IND, probe diameter of 1.3 cm) was used to measure reflectance with an Avantes Sensline spectrograph (AvaSpec-ULLS-TEC, range 300–1100 nm). The samples were analyzed with a 25 s integration time with an average number of 10 individual spectra collections. We placed the probe perpendicular to the samples. The Kubelka-Munk function (eq.2) [31], was used to convert the diffuse reflectance spectrum of each solid sample into the absorption spectrum $F(R)$, where R is the sample reflectance, and K and S are the absorption and scattering coefficients, respectively.

$$F(R) = \frac{(1-R)^2}{2R} = \frac{K}{S} \quad (2)$$

Computational details. Previously [16], to gain insight into the structure of **MSS** in solution and in the solid state, we have optimized the structures of its possible conformers and tautomers at the density functional theory (DFT) B3LYP/6–311++G(d,p**)** level of theory, both in the gas phase (isolated molecule in vacuum) and considering the bulk solvent effects of water and DMSO. The keto-enamine form **I-b-NH** was found to be the most stable structure (Scheme 2), followed by a second keto-enamine tautomer, while the enol-imine **III-c-OH** appears as the third most stable form in water (Scheme 2), as well as in DMSO [16]. Additional calculations for the **Al(III)/MSS** complex revealed that the most stable form for this species is the one represented in Scheme 2 (named conformer **I**) [16]. Based on these structures, time-dependent DFT (TD-DFT) calculations were now carried out using Gaussian 16 [32], and the long-range corrected CAM-B3LYP [33] Coulomb-attenuated functional (which has been shown to give accurate vertical excitation energies for a wide range of organic molecules) [34], and B3LYP [35–37], along with the 6–311++G(d,p) basis set. We conducted this study to identify the lowest singlet excited states of **MSS** and **Al(III)/MSS**, as well as their vertical excitation energies, oscillator strengths, and main contributions to the excited states. These calculations were undertaken in water solvent, simulated using the IEF-PCM model [38,39].

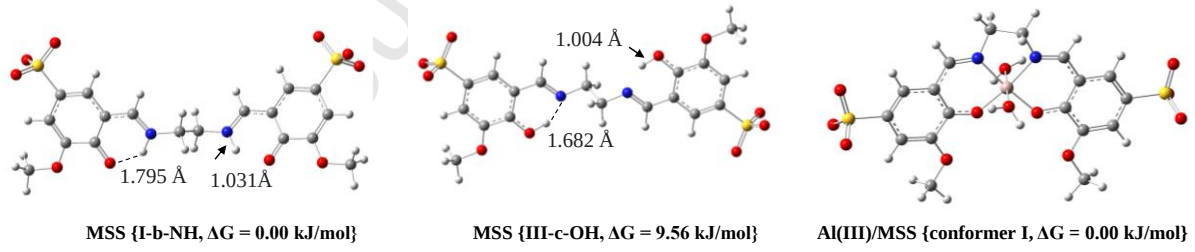

Scheme 2. DFT(B3LYP)/6–311++G(d,p) optimized geometries of the most stable conformers, keto-enamine form (I-b-NH) and enol imine form (III-c-OH) of **MSS**, and **Al(III)/MSS** complex (conformer I), considering the bulk effects of water solvent [16].

Photocatalytic activity. A degradation study was conducted to evaluate the photocatalytic efficiency of the synthesized **Al(III)/MSS** complex for the degradation of methylene blue (MB) under UV light. For the experiment, 20 mg of the **Al(III)/MSS** catalyst

was added to 40 mL of an aqueous MB solution with an initial concentration of C_o = 1.75 × 10^{-5} mol dm^{-3}, and the mixture was transferred to a beaker. Prior to UV irradiation, the suspension was magnetically stirred in the dark for 40 minutes to establish adsorption–desorption equilibrium between the dye molecules and the catalyst surface. The reaction mixture was then exposed to UV irradiation using an Accled Photoreactor M2 equipped with a 365 nm LED UV light source (power 1.5 W total radiant flux at 100 % intensity), while the LED intensity was set to 50 %, maintaining continuous magnetic stirring at 200 rpm. The degradation process was monitored over various irradiation times to assess the photocatalytic performance of the complex. A photolysis test was conducted under identical conditions in the absence of the photocatalyst.

Photocatalytic experiments were also carried out in the presence of three radical scavengers to identify the predominant reactive species involved in the photocatalytic degradation of MB. Ethylenediaminetetraacetic acid disodium salt 2-hydrate (EDTA), p-benzoquinone (BQ), and ethanol (EtOH) were used as scavengers for photogenerated holes (h^+), superoxide radicals ($O_2^{\bullet -}$), and hydroxyl radicals ($OH^{\bullet}$), respectively. Each scavenger was added at a concentration of 0.5 mM, and the reaction mixtures were subsequently analyzed by UV–vis spectroscopy.

The photocatalytic efficiency (%) was calculated using the formula,

$$\%\ \text{Degradation} = \frac{A_0 - A_t}{A_0} * 100 \qquad (3)$$

where A_0 and A_t are, respectively, the absorbance of the MB solution before and after t minutes of the photocatalytic reaction.

Results and discussion

1. *Absorption properties of **SS**, **MSS** and **Al(III)/MSS***

In our previous study [16], a thorough speciation and structural characterization of the **Al(III)/MSS** complex was carried out in solution, using multinuclear NMR, and in the solid state, using Raman and infrared spectroscopies, supplemented with DFT calculations. In the present work, we extended our research using UV-vis absorption spectroscopy to analyze the interactions between **MSS** and Al(III). The electronic spectra of 5 × 10^{-5} mol dm^{-3} aqueous

solutions of **MSS** and **Al(III)/MSS** were registered in water, and the wavelengths corresponding to the absorption maxima are listed in Table 1. TD-DFT calculations were carried out for both **MSS** and **Al(III)/MSS** in water to assist in the assignment of electronic bands and tautomers, as well as in the interpretation of their spectra. The B3LYP functional was utilized to perform this analysis since it was found to reproduce very well the electronic spectrum of the **MSS** Schiff base. In particular, it demonstrated a significant improvement over CAM-B3LYP (Figure S1 and Table S1), in spite of the fact that CAM-B3LYP produces quantitatively accurate results in the simulation of the electronic spectrum of **Al(III)/MSS**. The calculated transition energies, converted to wavelengths, and oscillator strengths for the enol form (**III-c-OH** conformer) and the keto form (**I-b-NH** conformer) of the ligand, as well as for conformer **I** of the **Al(III)/MSS** complex are listed in Table 1 and shown in Figure 1, where they are also compared with the experimental spectra.

As shown in Table 1 and Figure 1, the calculations predict an absorption band at 410 nm for the ligand **MSS** (keto **I-b-NH** form), which corresponds to the experimental band observed at 406 nm. This band is due to HOMO–LUMO excitation of the ligand and has $\pi \rightarrow \pi^*$ character (Figure S2). It clearly identifies the presence of the keto-enamine form, as this band is absent from the theoretical spectrum of the enol-imine tautomer (Figure 1). The absorption band located at 292 nm (predicted at 295 nm) is assigned to transitions from HOMO–2 and HOMO–4 to LUMO, and it is also ascribable to the keto-enamine form (Figure S2). Finally, the experimental band at 248 nm can be assigned to both the band predicted at 247 nm for the **I-b-NH** form and the band predicted at 234 nm for the **III-c-OH** conformer (Figures S2 and S3). These results indicate that the Schiff base **MSS** exists predominantly in the keto form in aqueous solution, with a minor contribution from the enol form. The good agreement between the calculated and experimental absorption spectra validates the computational approach and allows a high degree of confidence in the predictions of the tautomeric distribution in solution.

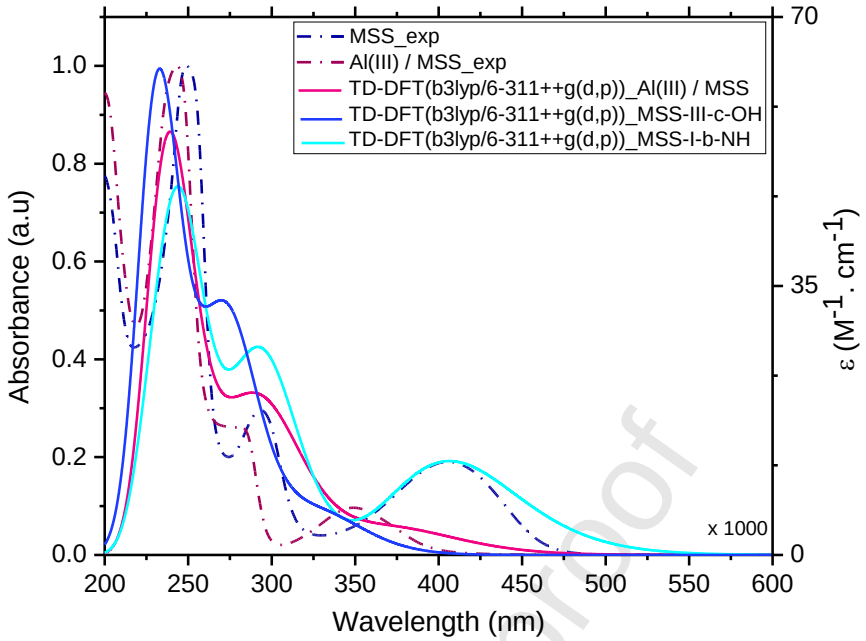

Figure 1. Experimental and calculated (TD-DFT B3LYP/6-311++G(d,p)) absorption spectra of **MSS** and **Al(III)/MSS** complex (H_2O).

For the **Al(III)/MSS** complex, a strong absorption band has been calculated at 356 nm (S_3 excited state), which corresponds to the experimental band found at 349 nm. This band involves electronic excitation from the HOMO to the LUMO+1 orbitals with $\pi \rightarrow \pi^*$ character. The performed calculations predict a blue shift of around 54 nm in the absorption maximum due to complexation, which is consistent with the experimental blue shift of 57 nm found when comparing the experimental absorption maxima for the ligand and complex [40]. In perfect agreement between theoretical and experimental data, the **Al(III)/MSS** complex also exhibits a transition at 277 nm (predicted at 276 nm) from the HOMO–4 to the LUMO+1, and a transition at 243 nm (predicted at 236 nm) from the HOMO–1 and HOMO to the LUMO+5 and LUMO+4 orbitals, respectively, with $\pi \rightarrow \pi^*$ character (Figure S4).

The stability of the **Al(III)/MSS** complex was initially analyzed through UV-vis spectroscopy. The solution was stored in the dark, and the absorption spectra remained unchanged after 24 hours, indicating that the compound is stable in solution. For additional information on the stability of **Al(III)/MSS** in more concentrated solutions (~5 mmol dm^{-3}), a series of NMR measurements in D_2O were carried out over the same period (Figure S5),

revealing no observable changes, thereby providing additional evidence of the complex's stability.

Table 1. Vertical excitation energies (in eV), oscillator strengths (*f*), wavelengths (λ), and major contributions calculated for **MSS** and **Al(III)/MSS** complex (TD-DFT B3LYP/6-311++G(d,p), IEFPCM (H_2O)) [38,39].

Excited state	Energy (eV)	$\lambda_{calc.}$ (nm)	$\lambda_{exp.}$ (nm)	f^a	Major Contributions (%)
					MSS (I-b-NH)
S_1	3.02	410	406	0.22	HOMO→LUMO (91%)
S_2	3.09	402	406	0.06	HOMO–1→LUMO (89%)
S_9	4.20	295	292	0.58	HOMO–4→LUMO (50%) + HOMO–2→LUMO (44%)
S_{19}	5.01	247	248	0.88	HOMO–8 →LUMO (19%) + HOMO–1→LUMO+2 (22%) + HOMO→LUMO+3 (46%)
					MSS (III-c-OH)
S_1	3.31	375	330	0.12	HOMO–1→LUMO+1 (25%) + HOMO→LUMO (75%)
S_5	4.51	275	-	0.62	HOMO–2→LUMO (87%)
S_{15}	5.30	234	248	0.81	HOMO–1→LUMO+3 (32%) + HOMO–1→LUMO+4 (25%) + HOMO→LUMO+3 (27%) + HOMO→LUMO+5 (16%)
					Al(III)/MSS
S_1	3.13	396	-	0.01	HOMO→LUMO (97%)
S_2	3.21	386	-	0.04	HOMO–1→LUMO (100%)
S_3	3.47	356	349	0.03	HOMO →LUMO+1 (100%)
S_5	4.05	306	-	0.03	HOMO–3→LUMO+1 (29%) + HOMO–2→LUMO (71%)
S_7	4.08	303	-	0.25	HOMO–4→LUMO (100%)
S_{11}	4.47	276	277	0.10	HOMO–4→LUMO+1 (86%)
S_{25}	5.25	236	243	0.15	HOMO–1→LUMO+5 (28%) + HOMO→LUMO+4 (72%)

[a] Results are shown for the region of energy up to 5.30 eV and calculated oscillator strength > 0.01.

UV-vis absorption spectroscopy was also used to study the effects of the methoxy substituent and the solvent dielectric constant on the tautomeric preferences of **MSS** in solution. This provides insight into how electronic and solvation effects modulate the relative stability and population of tautomeric forms, relevant in the design of molecules with tailored optical or chemical properties. **MSS** is soluble in water, DMSO, DMF and MeOH, and slightly soluble in less polar organic solvents [16]. The absorption spectra of **MSS**, and also of its non-methoxy substituted analogue, **SS**, were obtained in different solvents (H_2O, DMF, DMSO, and

methanol) at room temperature, and the wavelengths corresponding to the observed absorption maxima are listed in Table 2. In polar aprotic solvents, **SS** displays a broad weak absorption band at 415 and a strong band at 323 nm (in DMF), assigned to the keto and enol forms, respectively. These bands are observed at 420 and 336 nm in DMSO. The presence of intense bands at shorter wavelengths (below 400 nm) in the investigated solvents indicates that **SS** is mostly found in the enol-imine form. On the other hand, **MSS** exhibits relatively intense bands at 425 and 336 nm in DMF and at 430 and 337 nm in DMSO. Those bands mainly correspond to the $\pi \rightarrow \pi^*$ transitions of the intraligand charge transfer (ILCT) and the $n \rightarrow \pi^*$ transitions of the azomethine (–CH=N–) group (Figures S2 and S3). The observed bathochromic shift and the higher intensity of the absorption bands above 400 nm in **MSS** relative to **SS** can be attributed to the combined effects of the electron-donating methoxy ($-OCH_3$) substituent and dipole-dipole interactions as the substitution with the methoxy group increases the electronic density on the imine bond [41], further stabilizing the keto-enamine tautomer in these solvents. In polar protic solvents, the corresponding absorption bands of **SS** have maxima at 401 and 318 nm, in methanol, and at 388 and 316 nm, in water. Likewise, **MSS** has bands at 415 and 336 nm, in methanol, and at 406 and 292 nm, in water. In fact, when **MSS** dissolves in a protic solvent, such as methanol, the establishment of H-bonds between the carbonyl oxygen of **MSS** and the solvent disrupt the intramolecular N–H···O bonds, preventing the H transfer between the NH and the carbonyl that would contribute to stabilize the enol form. The result is a stabilization of the keto-enamine form [14,42].

According to the above results, we can infer that **MSS** is predominantly found in the keto form in the investigated protic solvents, while both the keto and enol forms coexist in significant amounts in the aprotic polar solvents. These findings are in accordance with DFT calculations, where the keto form **I-b-NH** was predicted as the most stable conformer in water, as well as in DMSO [16].

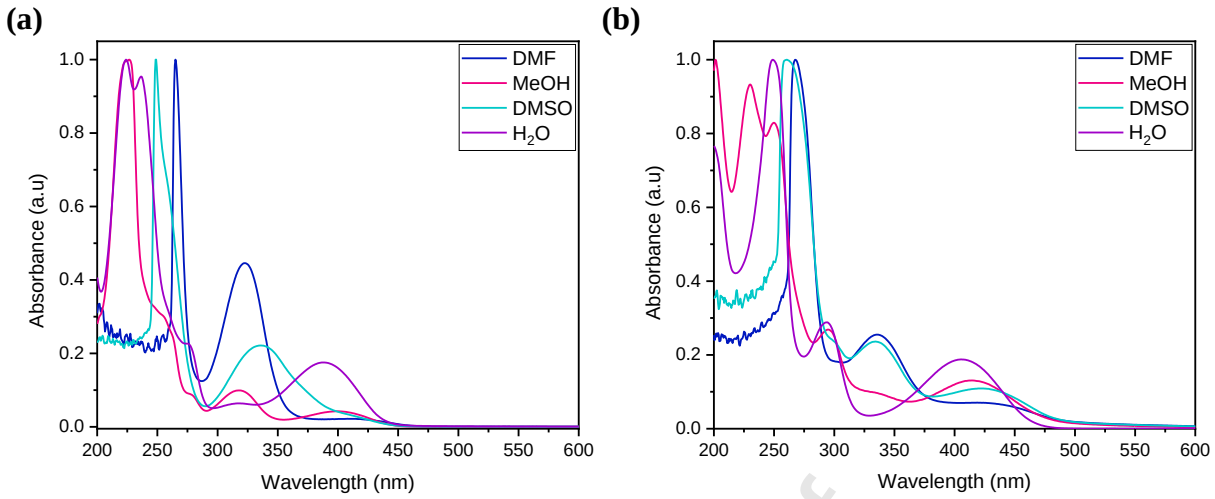

Figure 2.

Figure 2. Normalized electronic absorption spectra of **SS** (a) and **MSS** (b) in various solvents (5×10^{-5} mol dm^{-3}).

Table 2. Optical properties of **SS**, **MSS** and **Al(III)/MSS** complex measured in DMSO, DMF, MeOH, water and in the solid state.

Solvent	**SS**	**MSS**	**Al (III)/MSS**
	λ_{abs} (nm)	λ_{abs} (nm)	λ_{abs} (nm)
Dimethylsulfoxide (DMSO)	420, 336	430, 337, 300	364, 286
Water (H_2O)	388, 316, 274,236, 224	406, 292, 248	349,277,243
Dimethylformamide (DMF)	415, 323	425, 336	-
Methanol (MeOH)	401, 318, 277, 255, 226	415, 336, 295, 250, 230	-
Solid state	432, 403, 330, 310	452, 419, 390, 360, 320, 294	392, 355, 289

The photophysical properties of **SS**, **MSS**, and **Al(III)/MSS** complex were further studied using solid-state diffuse reflectance spectroscopy (DRS). The reflectance spectrum has been converted into the absorption spectrum $F(R)$ using the Kubelka-Munk (K−M) function [31] (Figure 3, eq. 2). The $F(R)$ spectra display distinct absorption edges and multiple peaks, which were deconvoluted and identified as electronic transitions using multi-peak Gaussian fitting.

Particularly noticeable redshifts were observed upon going from solution to the solid state, where **SS** exhibits absorption bands at 432, 403, 330, and 310 nm, while **MSS** reveals an even more redshifted pattern with maxima at 452, 419, 390, 360, 320, and 294 nm. Those bands may be attributed to $\pi \rightarrow \pi^*$ transitions of the phenyl rings and the $n \rightarrow \pi^*$ transitions of the azomethine (–CH=N–) group. The significant bathochromic changes observed in both compounds imply that intramolecular interactions are responsible for maintaining the keto-enamine tautomer when solvent-solute interactions are absent. Notably, the electron-donating methoxy (-OCH_3) group further improves conjugation, confirming the intramolecular charge

transfer and shifting absorption bands to even higher wavelengths, as evidenced by the larger redshifts seen for **MSS** as compared with its non-methoxy substituted analogue **SS**. In addition to intramolecular effects, intermolecular interactions such as hydrogen bonding or electrostatic interactions in the solid may also contribute to the observed spectral changes.

Upon complexation of **MSS** with Al(III), significant changes in the electronic structure are shown by the blue shifting (~60 nm) of the lowest energy absorption band in the **Al(III)/MSS** complex to 392 nm (Figure 3), corresponding to a $\pi \rightarrow \pi^*$ transition, in complete agreement with the DFT findings. Comparable results have been reported previously for analogous Schiff base complexes and their photophysical properties [40].

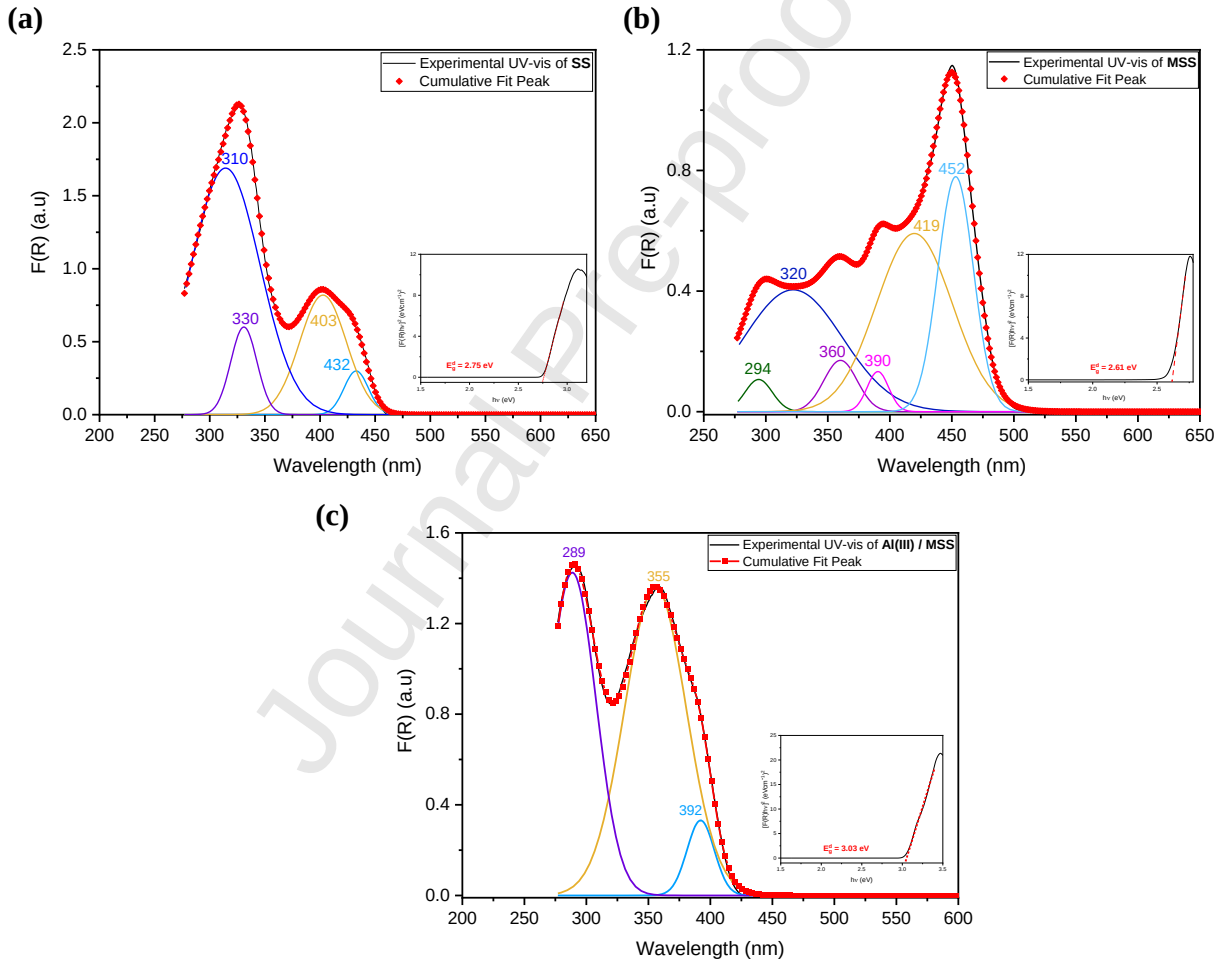

Figure 3. Multipeak Gaussian Fitting of the KM absorption F(R) of (a) **SS**, (b) **MSS** and (c) **Al(III)/MSS** (Inset-corresponding Tauc plots of direct gap energies, where the linear region is extrapolated to the x-axis to extract the estimated band gap energies (red lines))

The Tauc relation (eq. 4) was used to estimate the direct band gap energies of **SS**, **MSS**, and the **Al(III)/MSS** complex.

$$[F(R).h\nu]^{1/n} = B(h\nu - Eg) \quad (4)$$

In Eq. 4, B is a constant, ν is the photon frequency and h is the Planck's constant; n is equal to ½ for a direct allowed transition type. As illustrated in the inset of Figure 3, the direct band gap energies determined through the linear extrapolation of $(F(R)\cdot h\nu)^2$ values to zero absorption are 2.75 eV for **SS**, 2.61 eV for **MSS** and 3.03 eV for **Al(III)/MSS**, revealing their wide band gap semiconductor character, and making the compounds prospective candidates for use in optoelectronics.

To further evaluate the accuracy of the used theoretical methods, we have calculated the band gap energies of **MSS** and its Al(III) complex by using DFT. According to Koopman's theorem, the electronic band gap (E_g) can be estimated by the difference between the energy of the (Hartree-Fock or Kohn-Sham) highest occupied molecular orbital (HOMO) and that of the lowest unoccupied molecular orbital (LUMO). However, the exchange-correlation functional strongly affects these values, since they solely depend on the ground-state one-electron Kohn-Sham eigenvalues. A more precise method for determining E_g has been described by Cho et *al*. and involves utilizing the calculated energy difference between the vertical (or adiabatic) ionization potential (IP) and electron affinity (EA) (Scheme 3) [43]. The DFT electronic and optical band gap energies (E_g and O_g, respectively) are compared with the experimentally determined O_g value in Table 3, showing that the adiabatic results allow a rather good reproduction of the experimental data, suggesting that the structural relaxation process may be relevant. Previous reports have shown that improved photocatalytic efficiency is correlated with a narrower band gap.

Table 3. Experimental and (vertical, v, or adiabatic, ad) calculated optical band gap O_g (eV), electronic band gap E_g (eV) and exciton binding energy, ΔE_{ex} (eV), obtained at the B3LYP/6-311++G(d,p) level in water.

	E_g (Calc.)		O_g (Calc.)		ΔE_{ex} (Calc.)		O_g (Exp.)
	$E_{g,v}$ (Calc.)	$E_{g,ad}$ (Calc.)	$O_{g,v}$ (Calc.)	$O_{g,ad}$ (Calc.)	$\Delta E_{ex,v}$ (Calc.)	$\Delta E_{ex,ad}$ (Calc.)	-
MSS (**I-b-NH**)	3.15	2.84	3.02	2.72	0.13	0.12	2.61
Al(III)/MSS	3.38	3.07	3.13	2.86	0.25	0.21	3.03

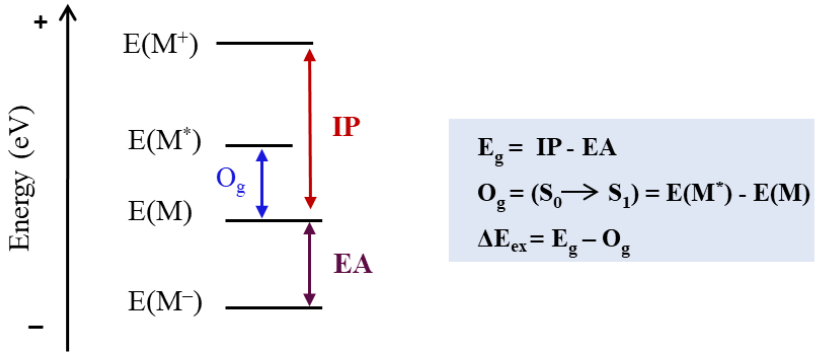

Scheme 3. Scheme illustrating the definition of the vertical (or adiabatic) ionization potential (IP = $E(M^+)_M$ – E(M)), electron affinity (EA = E(M) – $E(M^-)_M$), electronic (or fundamental) band gap (E_g = IP – EA), optical band gap ($O_g = E(M^*)_M$ – E(M)) and exciton binding energy ($\Delta E_{ex} = E_g - O_g$). In these definitions, E(M) denotes the energy of the ground state S_0 at the optimized geometry, and $E(M^*)_M$, $E(M^+)_M$ and $E(M^-)_M$, denote the energy of the S_1 excited state and those of the cation and anion, respectively, at the S_0 optimized geometry (vertical calculation) or using the relaxed geometry of each species at each electronic state (adiabatic calculation) [43].

2. *Photoluminescence properties of **MSS** and **Al(III)/MSS***

In this section, we report on the solid-state photoluminescence properties of **MSS** and **Al(III)/MSS** at room temperature. Figure 4 illustrates the emission spectra taken at different excitation energies, namely at 2.70 eV (460 nm), 2.77 eV (447 nm) and 3.07 eV (404 nm) for **MSS**, and at 2.70 eV (460 nm), 3.06 eV (405 nm), 3.17 eV (392 nm) and 3.49 eV (355 nm) for the **Al(III)/MSS** complex. Table 4 displays the obtained chromaticity coordinates (x, y), color purity (CP) and associated color temperature (CCT) for both compounds emission under the different excitations, which were calculated using well-stablished methods [44]. For the Schiff base **MSS**, excitation at longer wavelengths (404→460 nm), leads to a notable increase in color purity (CP) from 42% to 68%. Meanwhile, chromaticity coordinates shift from (0.30, 0.47) to (0.34, 0.56), while CCT decreases from 6367 K to 5372 K, indicating cool white-light emission. Indeed, **MSS** exhibits broad luminescence bands centered at 516-521 nm, ascribable to the π-π^* transitions of the aromatic rings. Even though **MSS** emission is not as pure (CP = 42-68%) as the one of commercial tris(2-phenylpyridine)iridium(III) ($Ir(ppy)_3$), the luminescent organometallic complex of iridium(III) most widely used in optoelectronics, particularly as a green phosphorescent organic light-emitting diode (OLED), which has CP = 85%, the metal-free design of **MSS** and excitation tunability makes it cost-effective as a supplementary green emitter.

In comparison to the free ligand **MSS**, the Al(III) complex exhibits the opposite behaviour: when excitation wavelength increases from 355 to 460 nm, the CP as well as CCT decreases significantly from 29% to 12% and from 21392 K to 9175 K, respectively, while the

chromaticity shifts from (0.21, 0.28) to (0.27, 0.33), indicating a cooler, bluish-white light emission. Upon excitation at 460 nm, the **Al(III)/MSS** complex displays a broad emission spectrum that covers the entire visible region, with (0.27, 0.33) coordinates that are closer to the pure-white light emission (0.33, 0.33). Upon excitation at 3.06-3.49 eV (405-355 nm), **Al(III)/MSS** emits an effective blue luminescence. Kumar et al. demonstrated that white light emission can be achieved through the conjugated use of an orange dye and blue light-emitting materials, which serve as dopants [45]. The tunable blue-white emission of the synthesized Al(III) complex thus confers to this material potential for application in single layer white OLEDs. However, its relatively low CP (12-29%) suggests limited efficiency, highlighting the need to optimize energy transfer mechanisms for improved performance.

In addition to their optical properties, the Schiff base **MSS** exhibits a decomposition temperature of 239 °C, while its Al(III) complex shows enhanced thermal stability with a decomposition temperature of 281 °C, as determined by DSC [16]. These results suggest that both compounds possess sufficient thermal stability for potential use in single-layer OLED devices.

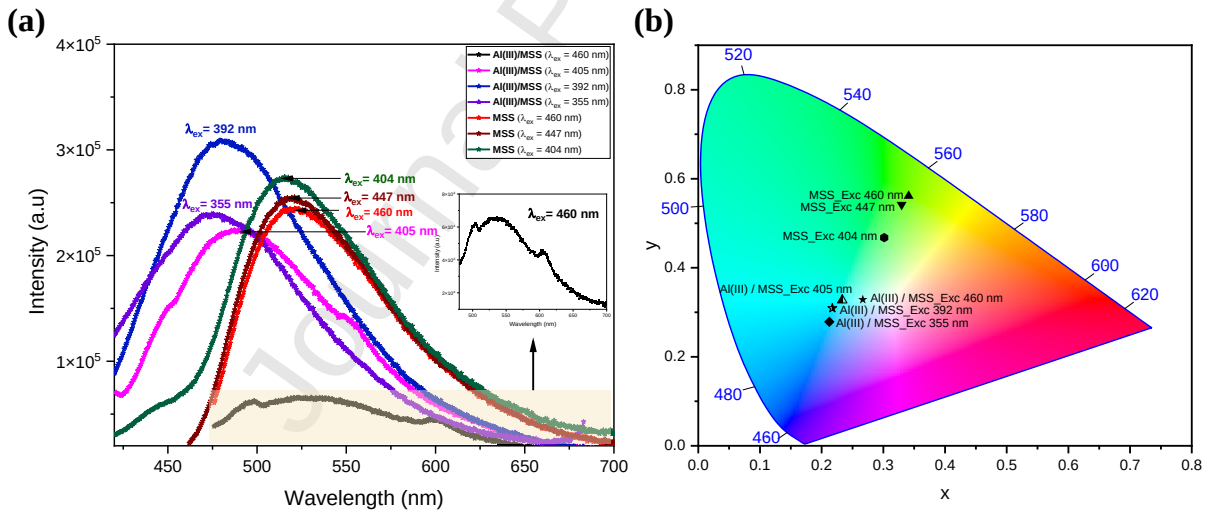

Figure 4. (a) Emission spectra of **MSS** (under different excitations at 404, 447, and 460 nm), and **Al(III)/MSS** (under different excitations at 355, 392, 405 and 460 nm), (b) CIE chromaticity coordinates of **MSS** and **Al(III)/MSS**.

Table 4. Chromaticity coordinates (x,y), correlated color temperature (CCT) and color purity (CP) of **MSS** and **Al(III)/MSS**

MSS				**Al(III)/MSS**			
λ_{ex} (nm)	(x, y)	CCT	CP (%)	λ_{ex} (nm)	(x, y)	CCT	CP (%)
404	(0.30, 0.47)	6367	42	355	(0.21, 0.28)	21392	29
447	(0.33, 0.54)	5556	62	391	(0.22, 0.31)	14953	25
460	(0.34, 0.56)	5372	68	405	(0.23, 0.33)	12327	22

-	-	-	-	460	(0.27, 0.33)	9175	12

Fluorescence quantum yields for **MSS** and its Al(III) complex were determined in solution using quinine sulfate in 0.5 mol dm^{-3} sulfuric acid (Φ_F = 0.55) as the standard [30]. The Φ_F value obtained in water for **Al(III)/MSS** is 0.008, and this value increases to 0.050 upon changing the solvent to DMSO. For **MSS**, the Φ_F value measured in DMSO is 0.049.

*3. Photocatalytic activity of **Al(III)/MSS***

As discussed above, the **Al(III)/MSS** complex has a narrow band gap, which is a critical factor determining the photon energy required for photocatalytic dye degradation. This characteristic indicates that the complex could serve as a promising material for photocatalytic applications. This motivated us to investigate the photocatalytic activity of the synthesized **Al(III)/MSS** complex against the methylene blue (MB) dye in aqueous solution under UV light irradiation. The changes in MB concentration were monitored spectroscopically over a period of 70 min, in the absence (Figure 5(A)) and presence of **Al(III)/MSS** catalyst (Figure 5(B)). As the irradiation time increases, in the absence of a photocatalyst, MB is observed to experience 35% photodegradation, which could be a result of photolysis. Noteworthy, in the presence of the catalyst, this value increases to 96 % (Figure 5(C)). To the best of our knowledge, this is the first water-soluble Schiff base Al(III) complex shown to be an efficient photocatalyst for the studied reaction. Previously, Ni(II), Co(II) and Cu(II) Schiff base complexes have been found to be able to catalyze the photodegradation of MB, but, with a single exception, with a considerably lower efficiency than the presently described Al(III) complex (Table 5) [46–48].

Based on the Langmuir–Hinshelwood model, the pseudo-first-order kinetics equation was tested (eq. 5), where C_0 and C_t are, respectively, the concentration of the MB solution before and after t minutes of the photocatalytic reaction and k is the rate constant of the pseudo-first order reaction. Figure 5(D) illustrates the kinetics of the photodegradation of MB in the presence of **Al(III)/MSS**. A linear plot of $\ln(C_0/C_t)$ *vs.* time with high correlation coefficient values (R^2 = 0.986) and rate constant (k) of 0.032 min^{-1} confirms that the degradation process follows first-order kinetics. The calculated rate constant (k) shows that the synthesized complex has considerable photoreactive potential when exposed to UV light, indicating that it is an effective catalytic agent.

$$ln\left(\frac{C_0}{C_t}\right) = kt \qquad (5)$$

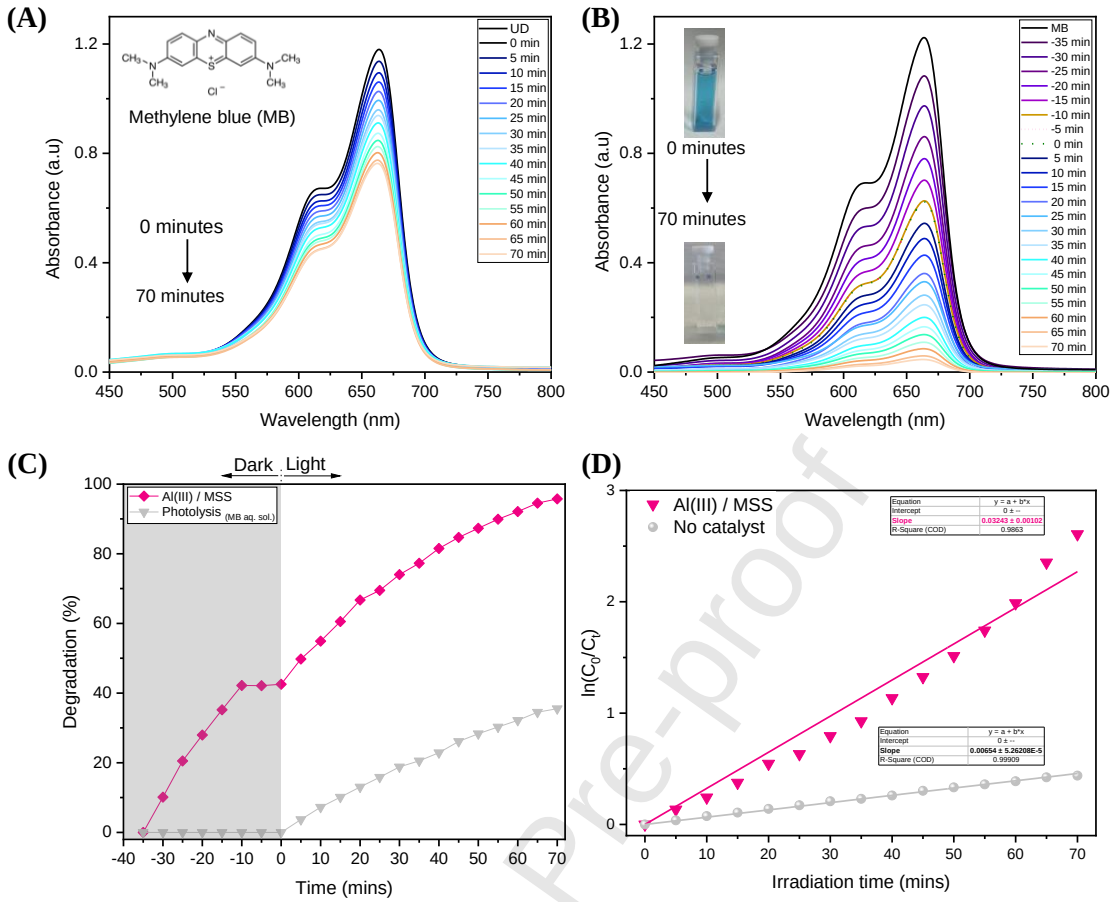

Figure 5. Photocatalytic degradation of a 5.6 mg L^{-1} MB aqueous solution: (A) in the absence and (B) in the presence of the **Al(III)/MSS** catalyst under UV irradiation; (C) percentage of MB degradation with and without the catalyst; (D) reaction order of the photocatalytic degradation process of MB by **Al(III)/MSS**. Experimental conditions: Temp. = 298.15 K, pH 4, catalyst mass = 20 mg, and pollutant solution volume = 40 mL.

Table 5. Summary of the photocatlytic degradation of methylene blue (MB) in the presence of different transition metal-Schiff base complexes in comparison with our **Al(III)/MSS** complex.

Catalyst	Mass of Catalyst (mg)	Polluant concentration (mol dm^{-3})	Irradiation time	Light source	Degradation efficiency (%)	Rate constant k (min^{-1})	Ref.
$Cu(L_2)$	35	4.70×10^{-5}	150 min	UV lamp (25 W)	50 %	0.0026	[46]
$Cu_2(HL)_2(N_3)_2$	35	4.70×10^{-5}	150 min	UV lamp (25 W)	52 %	0.0038	[46]
$Cu(HL)_2(SO_4)$	35	4.70×10^{-5}	150 min	UV lamp (25 W)	51 %	0.0036	[46]
$Ni(L_2)$	20	3.13×10^{-5}	60 min	UV light (320 nm)	76.50 %	-	[47]
$Co(L_2)$	10	3.13×10^{-5}	90 min	UV light (320 nm)	64.40 %	-	[47]

Cu(CPAMN)	30	5.00×10^{-4}	30 min	Visible light	56 %	0.0272	[48]
Cu(FPAMN)	30	5.00×10^{-4}	30 min	Visible light	97 %	0.1207	[48]
Al(III)/MSS	20	1.75×10^{-5}	70 min	UV light (365 nm)	96 %	0.0324	This work

Reactive species trapping and mechanistic insights into the photocatalytic degradation of MB. The overall photocatalytic performance of the **Al(III)/MSS** complex depends on the efficient generation, separation, and migration of photogenerated charge carriers, as well as the subsequent redox reactions occurring at the catalyst surface. Therefore, a detailed scavenger study was conducted to gain deeper insight into the photocatalytic mechanism of the **Al(III)/MSS** system. This analysis was performed to clarify whether the photocatalytic degradation of methylene blue (MB) proceeds mainly through reactive oxygen species, such as hydroxyl radicals ($OH^{\bullet}$) and superoxide radicals ($O_2^{\bullet-}$), or through direct oxidation-reduction involving photogenerated holes (h^+) and electrons (e^-). Scavengers including ethanol (EtOH), *p*-benzoquinone (BQ), and ethylenediaminetetraacetic acid disodium salt 2-hydrate (EDTA) were employed as quenching agents for $OH^{\bullet}$, $O_2^{\bullet-}$, and h^+, respectively. In the absence of any scavenger, nearly complete degradation (~ 96 %) of MB was achieved after 70 min of UV light irradiation using the **Al(III)/MSS** photocatalyst (Figure 5(C)). However, the degradation efficiency significantly decreased upon the addition of these scavengers, dropping to 44% in the presence of EtOH, 56% with EDTA, and 81% with BQ (Figure 6). These observations indicate that hydroxyl radicals ($OH^{\bullet}$) play the predominant role in MB degradation in the presence of **Al(III)/MSS**, followed by photogenerated holes (h^+) and superoxide radicals ($O_2^{\bullet-}$).

A general mechanism for the photocatalytic process can be discussed based on our reactive species trapping study and current literature [49–51]. Upon UV light irradiation, the photocatalyst **Al(III)/MSS** absorbs photons, promoting electrons from the valence band (VB) to the conduction band (CB), leaving holes (h^+) in the VB (Eq. 6). Although the exact CB and VB edge positions of the photocatalyst were not determined, the major role of hydroxyl radicals in the photocatalytic process suggests that the photogenerated holes possess sufficient oxidative potential to oxidize adsorbed H_2O or OH^- and generate $OH^{\bullet}$ radicals (Eq. 7). Additionally, the contribution of $O_2^{\bullet-}$ in the photocatalysis confirms that CB electrons can effectively reduce adsorbed O_2 to form $O_2^{\bullet-}$ radicals (Eq. 8). These species undergo subsequent

reactions yielding $HO_2^{\bullet}$, H_2O_2, and additional $OH^{\bullet}$ radicals (Eqs. 9–11). The generated reactive oxygen species oxidize MB molecules, leading to their degradation and, possibly, mineralization into CO_2, inorganic ions and H_2O (Eqs. 12–13). Therefore, the results of the scavenger test show that $OH^{\bullet}$ radicals are the main reactive species responsible for the degradation of MB, and provide evidence that both oxidation and reduction processes are involved in its degradation in the presence of **Al(III)/MSS**. Scheme 4 illustrates the photocatalytic process of the synthesized complex **Al(III)/MSS** against methylene blue.

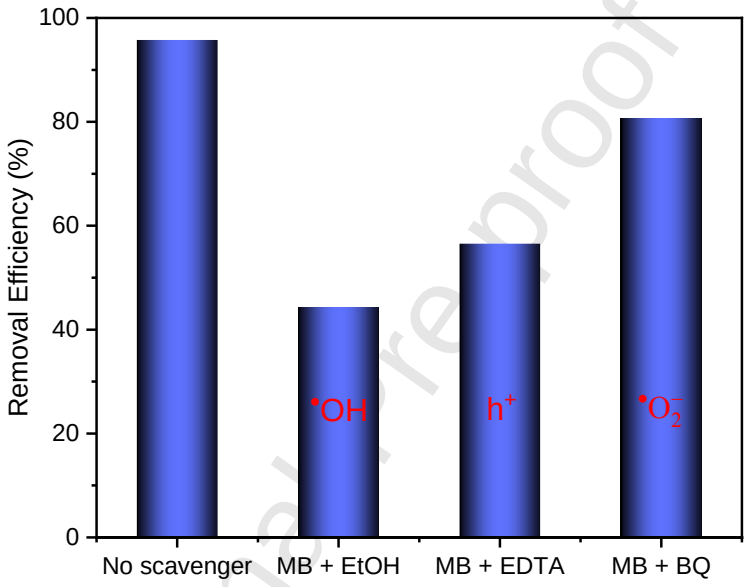

Figure 6. Photocatalytic degradation of a 5.6 mg L^{-1} MB aqueous solution by the **Al(III)/MSS** complex in the absence of scavengers and in the presence of hydroxyl radical scavenger (EtOH), hole scavenger (EDTA), and superoxide radical scavenger (BQ). Experimental conditions: temperature = 298.15 K; catalyst mass = 20 mg; pollutant solution volume = 40 mL.

$$\textbf{Al(III)/MSS} + h\nu \longrightarrow e^- (CB) + h^+ (VB) \quad (6)$$

$$h^+ (VB) + (H_2O)_{ads} \longrightarrow OH^{\bullet} + H^+ \quad (7)$$

$$(O_2)_{ads} + e^- (CB) \longrightarrow O_2^{\bullet -} \quad (8)$$

$$O_2^{\bullet -} + H^+ \longrightarrow HO_2^{\bullet} \quad (9)$$

$$2HO_2^{\bullet} \longrightarrow H_2O_2 + O_2 \quad (10)$$

$$e^- + H_2O_2 \longrightarrow OH^{\bullet} + OH^- \quad (11)$$

$$OH^{\bullet} + MB \longrightarrow \text{Degradation products} \quad (12)$$

$$O_2^{\bullet -} + MB \longrightarrow \text{Degradation products} \quad (13)$$

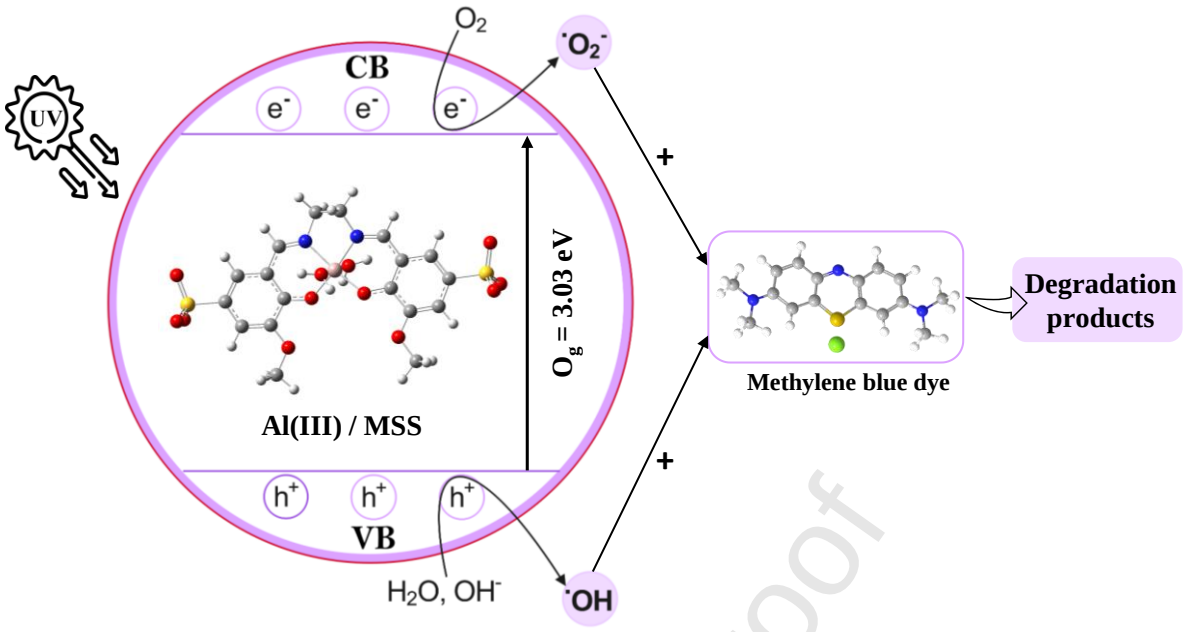

Scheme 4. Schematic of the expected mechanism for the photodegradation of methylene blue (MB) by **Al(III)/MSS** catalyst under UV light.

Conclusions

In this work, we investigated the photophysical properties of the water-soluble di-Schiff base *N*,*N*′-bis(3-methoxy-5-sulfonatosalicylidene)-1,2-ethylene-diamine disodium salt (**MSS**) and its Al(III) complex, both of which were synthesized and structurally characterized in our previous study. Using UV–vis absorption and diffuse reflectance spectroscopy, we conducted a comprehensive analysis of the tautomeric preferences (enol-imine vs. keto-enamine) of **MSS**, using its non-methoxy-substituted analogue **SS** as a reference compound for comparison across various solvents and in the solid state. **MSS** displays a notable bathochromic shift relative to **SS** in all media studied. Spectroscopic data indicate that the keto-enamine form is the predominant tautomer in protic solvents (H_2O, MeOH) and in the solid state, whereas a mixture of keto and enol forms coexist in aprotic polar solvents (DMSO, DMF). In contrast, **SS** exhibits a dynamic equilibrium between both forms in protic solvents, while the enol-imine form is favored in DMSO and DMF. The solid-state characterization (DRS) revealed that, in this phase, the Schiff base **SS** predominantly exists in the keto-enamine tautomeric form. These results provide insight into how electronic and solvation effects modulate the relative stability and population of tautomeric forms, relevant in the design of molecules with tailored optical or chemical properties.

Upon complexation with Al^{3+} ions, both the solution and solid-state absorption spectra of **MSS** undergo a hypsochromic shift, which aligns with theoretical predictions showing a calculated blue shift of 54 nm. The optical band gap energies were determined to be 2.75 eV for **SS**, 2.61 eV for **MSS**, and 3.03 eV for the **Al(III)/MSS** complex, confirming their classification as wide-bandgap semiconductors and suggesting their potential suitability for optoelectronic applications. These experimental values are well supported by DFT-calculated electronic and optical band gaps, which show good agreement with the observed data.

Photoluminescence analysis revealed that **MSS** emits in the green region, while its Al(III) complex shows blue-white emission, indicating their promise as single-layer white OLED materials. Beyond optoelectronic applications, we also explored the photocatalytic activity of the **Al(III)/MSS** complex. Under UV irradiation, the complex demonstrated 96% degradation efficiency toward methylene blue (MB), with a rate constant (k) of 0.032 min^{-1}. This water-soluble complex, based on an earth-abundant and affordable metal, presents a sustainable and economically viable alternative to photocatalysts derived from scarce and expensive metals, offering potential for large-scale environmental and optoelectronic applications.

Data availability

The data supporting this article has been included as part of the Supplementary Information.

Conflicts of interest

There are no conflicts to declare.

CRediT authorship contribution statement

Hajer Bouznif: Conceptualization, Methodology, Investigation, Formal analysis, Writing – original draft, Visualization, Validation, Writing – review & editing. **Licínia L. G. Justino:** Conceptualization, Methodology, Validation, Supervision, Writing – review & editing. **Telma Costa:** Validation, Writing – review & editing. **Maria I. L. Soares:** Methodology, Writing – review & editing. **M. Luísa Ramos:** Investigation, Writing - Review & Editing. **Teresa M. V. D. Pinho e Melo:** Validation, Resources, Writing - Review & Editing. **Nabil Zouari:** Writing – review & editing, Supervision, Project administration. **Rui Fausto:** Conceptualization, validation, Writing - Review & Editing, Supervision, Funding acquisition.

Acknowledgements

We acknowledge funding from the Coimbra Chemistry Centre – Institute of Molecular Sciences (CQC-IMS) which is supported by the Fundação para a Ciência e a Tecnologia (FCT), Portuguese Agency for Scientific Research. CQC is funded by FCT through projects UID/PRR/00313/2025 (https://doi.org/10.54499/UID/PRR/00313/2025) and UID/00313/2025 (https://doi.org/10.54499/UID/00313/2025) and IMS through special complementary funds provided by FCT (project LA/P/0056/2020 https://doi.org/10.54499/LA/P/0056/2020). The authors also thank the Laboratory for Advanced Computing at the University of Coimbra for providing computing resources that have contributed to the research results reported within this paper (URL: https://www.uc.pt/lca). The NMR data was collected at the UC-NMR facility (URL: www.nmrccc.uc.pt) which is supported in part by FEDER – European Regional Development Fund through the COMPETE Programme (Operational Programme for Competitiveness) and by national funds through FCT (Grants REEQ/481/QUI/2006, RECI/QEQ-QFI/0168/2012, CENTRO-07-CT62-FEDER-002012, and Rede Nacional de Ressonância Magnética Nuclear (RNRMN)). L.L.G.J. acknowledges the ReMade-at-ARI project (reference: 101058414), financed by European Union through the Horizon Europe Program (HORIZON-INFRA-2021-SERV-01-04) under Grant Agreement nº 101058414. The Horizon-Widera-2023-Talents-01 ERA-Chair 1011848998 Spectroscopy@IKU "*Manipulating and Characterizing Molecular Architectures: From Isolated Molecules to Molecular Crystals*" is Funded by the European Union.

References

[1] H. Schiff, Mittheilungen aus dem Universitätslaboratorium in Pisa: eine neue Reihe organischer Basen, Justus Liebigs Ann. Chem. 131 (1864) 118–119. https://doi.org/10.1002/jlac.18641310113.
[2] A.L. Berhanu, Gaurav, I. Mohiuddin, A.K. Malik, J.S. Aulakh, V. Kumar, K.-H. Kim, A review of the applications of Schiff bases as optical chemical sensors, TrAC, Trends Anal. Chem. 116 (2019) 74–91. https://doi.org/10.1016/j.trac.2019.04.025.
[3] S. Kagatikar, D. Sunil, Schiff Bases and Their Complexes in Organic Light Emitting Diode Application, J. Electron. Mater. 50 (2021) 6708–6723. https://doi.org/10.1007/s11664-021-09197-9.
[4] J.M. Abad, M. Revenga-Parra, T. García, M. Gamero, E. Lorenzo, F. Pariente, Interactions of Schiff-base ligands with gold nanoparticles: structural, optical and electrocatalytic studies, Phys. Chem. Chem. Phys. 13 (2011) 5668–5678. https://doi.org/10.1039/C0CP02164D.
[5] D.G. De Kowalewski, R.H. Contreras, E. Díez, A. Esteban, NMR J(C,C) scalar coupling analysis of the effects of substituents on the keto–enol tautomeric equilibrium in 2-OH-n-X-pyridines. An experimental and DFT study, Mol. Phys. 102 (2004) 2607–2615. https://doi.org/10.1080/00268970412331292902.
[6] R.F. Martínez, E. Matamoros, P. Cintas, J.C. Palacios, Imine or Enamine? Insights and Predictive Guidelines from the Electronic Effect of Substituents in H-Bonded Salicylimines, J. Org. Chem. 85 (2020) 5838–5862. https://doi.org/10.1021/acs.joc.0c00130.
[7] D. Yordanov, V. Deneva, A. Georgiev, A. Crochet, K.M. Fromm, L. Antonov, Indirect solvent assisted tautomerism in 4-substituted phthalimide 2-hydroxy-Schiff bases, Spectrochim Acta A Mol Biomol Spectrosc. 237 (2020) 118416. https://doi.org/10.1016/j.saa.2020.118416.

[8] Ç. Albayrak, G. Kaştaş, M. Odabaşoğlu, R. Frank, The prototropic tautomerism and substituent effect through strong electron-withdrawing group in (E)-5-(diethylamino)-2-[(3-nitrophenylimino)methyl]phenol, Spectrochim Acta A Mol Biomol Spectrosc. 114 (2013) 205–213. https://doi.org/10.1016/j.saa.2013.05.044.
[9] G. Kaştaş, Ç.A. Kaştaş, B.K. Kırca, C.C. Ersanlı, The effect of the change in substituents' positions on the formation of supramolecular networks and the solvent type/substituent dependence of prototropic behavior in three new o-hydroxy Schiff bases, J. Mol. Struct. 1200 (2020) 127109. https://doi.org/10.1016/j.molstruc.2019.127109.
[10] S.D. Chatziefthimiou, Y.G. Lazarou, E. Hadjoudis, T. Dziembowska, I.M. Mavridis, Keto Forms of Salicylaldehyde Schiff Bases: Structural and Theoretical Aspects, J. Phys. Chem. B 110 (2006) 23701–23709. https://doi.org/10.1021/jp064110p.
[11] M.J. Reimann, D.R. Salmon, J.T. Horton, E.C. Gier, L.R. Jefferies, Water-Soluble Sulfonate Schiff-Base Ligands as Fluorescent Detectors for Metal Ions in Drinking Water and Biological Systems, ACS Omega 4 (2019) 2874–2882. https://doi.org/10.1021/acsomega.8b02750.
[12] Z. Chen, S. Guieu, N.G. White, F. Lelj, M.J. MacLachlan, The Rich Tautomeric Behavior of Campestarenes, Chem. Eur. J. 22 (2016) 17657–17672. https://doi.org/10.1002/chem.201603231.
[13] Z. Hayvali, D. Yardimci, Synthesis and spectroscopic characterization of asymmetric Schiff bases derived from 4′-formylbenzo-15-crown-5 containing recognition sites for alkali and transition metal guest cations, Transit. Met. Chem. 33 (2008) 421–429. https://doi.org/10.1007/s11243-008-9060-4.
[14] M. Rocha, D.M. Gil, G.A. Echeverría, O.E. Piro, J.L. Jios, S.E. Ulic, Enol-imino–Keto-enamine Tautomerism in a Diazepine Derivative: How Decisive Are the Intermolecular Interactions in the Equilibrium? J. Org. Chem. 84 (2019) 11042–11053. https://doi.org/10.1021/acs.joc.9b01533.
[15] M. Palusiak, S. Simon, M. Solà, Interplay between Intramolecular Resonance-Assisted Hydrogen Bonding and Aromaticity in o-Hydroxyaryl Aldehydes, J. Org. Chem. 71 (2006) 5241–5248. https://doi.org/10.1021/jo060591x.
[16] H. Bouznif, L.L.G. Justino, M.I.L. Soares, T. Costa, M.L. Ramos, T. Nikitin, T.M.V.D. Pinho e Melo, N. Zouari, R. Fausto, Novel tetradentate N_2O_2 water-soluble Schiff Base and its Al(III) complex: Synthesis, structural characterization, and correlations between structure and stability against hydrolysis, J. Mol. Struct. 1331 (2025) 141581. https://doi.org/10.1016/j.molstruc.2025.141581.
[17] C.W. Tang, S.A. VanSlyke, Organic electroluminescent diodes, Appl. Phys. Lett. 51 (1987) 913–915. https://doi.org/10.1063/1.98799.
[18] A. Saeed, Mir.A.N. Razvi, N. Salah, Third-order nonlinear optical properties of the small-molecular organic semiconductor tris (8-Hydroxyquinoline) aluminum by CW Z-scan technique, Results in Phys. 24 (2021) 104162. https://doi.org/10.1016/j.rinp.2021.104162.
[19] O. Sevgili, S. Canlı, F. Akman, I. Orak, A. Karabulut, N. Yıldırım, Characterization of aluminum 8-hydroxyquinoline microbelts and microdots, and photodiode applications, J. Phys. Chem. Sol. 136 (2020) 109128. https://doi.org/10.1016/j.jpcs.2019.109128.
[20] C. Pérez-Bolívar, S. Takizawa, G. Nishimura, V.A. Montes, P. Anzenbacher, High-Efficiency Tris(8-hydroxyquinoline)aluminum (Alq_3) Complexes for Organic White-Light-Emitting Diodes and Solid-State Lighting, Chem. Eur. J. 17 (2011) 9076–9082. https://doi.org/10.1002/chem.201100707.
[21] V.A. Montes, R. Pohl, J. Shinar, P. Anzenbacher Jr., Effective Manipulation of the Electronic Effects and Its Influence on the Emission of 5-Substituted Tris(8-quinolinolate) Aluminum(III) Complexes, Chem. Eur. J. 12 (2006) 4523–4535. https://doi.org/10.1002/chem.200501403.
[22] K.Y. Hwang, M.H. Lee, H. Jang, Y. Sung, J.S. Lee, S.H. Kim, Y. Do, Aluminium–salen luminophores as new hole-blocking materials for phosphorescent OLEDs, Dalton Trans. (2008) 1818. https://doi.org/10.1039/b717754b.
[23] P.O. Oladoye, T.O. Ajiboye, E.O. Omotola, O.J. Oyewola, Methylene blue dye: Toxicity and potential elimination technology from wastewater, Results Eng. 16 (2022) 100678. https://doi.org/10.1016/j.rineng.2022.100678.
[24] V. Bharti, K. Vikrant, M. Goswami, H. Tiwari, R.K. Sonwani, J. Lee, D.C.W. Tsang, K.-H. Kim, M. Saeed, S. Kumar, B.N. Rai, B.S. Giri, R.S. Singh, Biodegradation of methylene blue dye in a batch and continuous mode using biochar as packing media, Environ. Res. 171 (2019) 356–364. https://doi.org/10.1016/j.envres.2019.01.051.
[25] E.A. El-Sharkawy, A.Y. Soliman, K.M. Al-Amer, Comparative study for the removal of methylene blue via adsorption and photocatalytic degradation, J. Colloid Interface Sci. 310 (2007) 498–508. https://doi.org/10.1016/j.jcis.2007.02.013.
[26] N. Kannan, M.M. Sundaram, Kinetics and mechanism of removal of methylene blue by adsorption on various carbons—a comparative study, Dyes and Pigments 51 (2001) 25–40. https://doi.org/10.1016/S0143-7208(01)00056-0.

[27] M.I. Din, R. Khalid, J. Najeeb, Z. Hussain, Fundamentals and photocatalysis of methylene blue dye using various nanocatalytic assemblies- a critical review, J. Clean. Prod. 298 (2021) 126567. https://doi.org/10.1016/j.jclepro.2021.126567.
[28] G. Ramalingam, N. Perumal, A.K. Priya, S. Rajendran, A review of graphene-based semiconductors for photocatalytic degradation of pollutants in wastewater, Chemosphere 300 (2022) 134391. https://doi.org/10.1016/j.chemosphere.2022.134391.
[29] M. Pavel, C. Anastasescu, R.-N. State, A. Vasile, F. Papa, I. Balint, Photocatalytic Degradation of Organic and Inorganic Pollutants to Harmless End Products: Assessment of Practical Application Potential for Water and Air Cleaning, Catalysts 13 (2023) 380. https://doi.org/10.3390/catal13020380.
[30] J.N. Miller, General considerations on fluorescence spectrometry, in: Standards in Flourescence Spectrometry, Springer Netherlands, Dordrecht, 1981: pp. 1–7. https://doi.org/10.1007/978-94-009-5902-6_1.
[31] D.P. Law, A.B. Blakeney, R. Tkachuk, The Kubelka–Munk Equation: Some Practical Considerations, J. Near Infrared Spectrosc. 4 (1996) 189–193. https://doi.org/10.1255/jnirs.89.
[32] M. J. Frisch, G. W. Trucks, H. B. Schlegel, G. E. Scuseria, M. A. Robb, J. R. Cheese-man, G. Scalmani, V. Barone, G. A. Petersson, H. Nakatsuji, et al., Gaussian 16, Revision B.01, Gaussian, Inc., Wallingford CT, 2016.
[33] T. Yanai, D.P. Tew, N.C. Handy, A new hybrid exchange–correlation functional using the Coulomb-attenuating method (CAM-B3LYP), Chem. Phys. Lett. 393 (2004) 51–57. https://doi.org/10.1016/j.cplett.2004.06.011.
[34] D. Jacquemin, E.A. Perpète, G.E. Scuseria, I. Ciofini, C. Adamo, TD-DFT Performance for the Visible Absorption Spectra of Organic Dyes: Conventional versus Long-Range Hybrids, J. Chem. Theory Comput. 4 (2008) 123–135. https://doi.org/10.1021/ct700187z.
[35] A.D. Becke, Density-functional exchange-energy approximation with correct asymptotic behavior, Phys Rev. A 38 (1988) 3098–3100. https://doi.org/10.1103/PhysRevA.38.3098.
[36] C. Lee, W. Yang, R.G. Parr, Development of the Colle-Salvetti correlation-energy formula into a functional of the electron density, Phys. Rev. B 37 (1988) 785–789. https://doi.org/10.1103/PhysRevB.37.785.
[37] S.H. Vosko, L. Wilk, M. Nusair, Accurate spin-dependent electron liquid correlation energies for local spin density calculations: a critical analysis, Can. J. Phys. 58 (1980) 1200–1211. https://doi.org/10.1139/p80-159.
[38] S. Miertuš, E. Scrocco, J. Tomasi, Electrostatic interaction of a solute with a continuum. A direct utilizaion of AB initio molecular potentials for the prevision of solvent effects, Chem. Phys. 55 (1981) 117–129. https://doi.org/10.1016/0301-0104(81)85090-2.
[39] J. Tomasi, B. Mennucci, R. Cammi, Quantum Mechanical Continuum Solvation Models, Chem. Rev. 105 (2005) 2999–3094. https://doi.org/10.1021/cr9904009.
[40] J. Qin, Z. Yang, Bis-Schiff base as a donor–acceptor fluorescent probe: Recognition of Al^{3+} ions in near 100% aqueous solution, J. Photochem. and Photobiol. A 303–304 (2015) 99–104. https://doi.org/10.1016/j.jphotochem.2015.02.008.
[41] C. Li, H. Xie, S. Zhou, H. Hu, G. Chen, Z. Wei, J. Jiang, J. Qin, Z. Zhang, Y. Kong, The structure-activity relationship for the electron-donating functional groups in hydrazone-linked COFs and their photocatalytic H2O2 production, Mater. Res. Bull. 173 (2024) 112697. https://doi.org/10.1016/j.materresbull.2024.112697.
[42] M. Theetharappan, M.A. Neelakantan, A Water-Soluble Schiff Base Turn-on Fluorescent Chemosensor for the Detection of Al^{3+} and Zn^{2+} Ions at the Nanomolar Level: Application in Live-Cell Imaging, J. Fluoresc. 31 (2021) 1277–1290. https://doi.org/10.1007/s10895-021-02756-7.
[43] D. Cho, K.C. Ko, O. Lamiel-García, S.T. Bromley, J.Y. Lee, F. Illas, Effect of Size and Structure on the Ground-State and Excited-State Electronic Structure of TiO_2 Nanoparticles, J. Chem. Theory Comput. 12 (2016) 3751–3763. https://doi.org/10.1021/acs.jctc.6b00519.
[44] C.S. McCamy, Correlated color temperature as an explicit function of chromaticity coordinates, Color Res. Appl. 17 (1992) 142–144. https://doi.org/10.1002/col.5080170211.
[45] A. Kumar, R. Srivastava, S.S. Bawa, D. Singh, K. Singh, G. Chauhan, I. Singh, M.N. Kamalasanan, White organic light emitting diodes based on DCM dye sandwiched in 2-methyl-8-hydroxyquinolinolatolithium, J. Lumin. 130 (2010) 1516–1520. https://doi.org/10.1016/j.jlumin.2010.03.022.
[46] P.H.F. Fasna, S. Sasi, T.K.B. Sharmila, C.S.J. Chandra, J.V. Antony, V. Raman, Photocatalytic remediation of methylene blue and antibacterial activity study using Schiff base-Cu complexes, Environ. Sci. Pollut. Res. 29 (2022) 54318–54329. https://doi.org/10.1007/s11356-022-19694-x.
[47] N.B. Gopal Reddy, P. Murali Krishna, N. Kottam, Novelmetal–organic photocatalysts: Synthesis, characterization and decomposition of organic dyes, Spectrochim. Acta A Mol. Biomol. Spectrosc. 137 (2015) 371–377. https://doi.org/10.1016/j.saa.2014.08.045.
[48] R. Vallavoju, R. Kore, R. Parikirala, M. Subburu, R. Gade, V. Kumar, M. Raghavender, P. Chetti, S. Pola, Synthesis and Characterization of New Tetradentate N_2O_2-Based Schiff's Base Cu (II) Complexes for Dye Photodegradation, Photochem 3 (2023) 274–287. https://doi.org/10.3390/photochem3020016.

[49] S. Latif, M. Saeed, M. Imran, A. Javaid, U. Hira, L. Mitu, Synthesis, Characterization, and Photocatalytic Activity of Mixed-Ligand Cerium(III) and Bismuth(III) Complexes, Journal of Chemistry 2022 (2022) 1–12. https://doi.org/10.1155/2022/6849793.
[50] D. Abdrabou, M. Ahmed, A. Hussein, T. El-Sherbini, Photocatalytic behavior for removal of methylene blue from aqueous solutions via nanocomposites based on Gd2O3/CdS and cellulose acetate nanofibers, Environmental Science and Pollution Research 30 (2023) 99789–99808. https://doi.org/10.1007/s11356-023-28999-4.
[51] F. Azeez, E. Al-Hetlani, M. Arafa, Y. Abdelmonem, A.A. Nazeer, M.O. Amin, M. Madkour, The effect of surface charge on photocatalytic degradation of methylene blue dye using chargeable titania nanoparticles, Sci Rep 8 (2018) 7104. https://doi.org/10.1038/s41598-018-25673-5.

Declaration of interests

☒ The authors declare that they have no known competing financial interests or personal relationships that could have appeared to influence the work reported in this paper.

☐ The authors declare the following financial interests/personal relationships which may be considered as potential competing interests:

Graphical abstract

Highlights

- Effect of methoxy substitution on tautomerism of Schiff base in solution and solid.
- Schiff base and its Al(III) complex are wide-band-gap-semiconductors.
- Photoluminescent Schiff base and Al(III) complex with potential for optoelectronics.
- Efficient UV-driven photocatalytic degradation of MB using an Al(III) complex.